Improving electrochemical hydrogen evolution of Ag@CN nanocomposites by synergistic effects with α-rich proteins

Daily Rodríguez-Padrón,[a¥] Alain R. Puente-Santiago, [a,b¥] Manuel Cano,[c] Alvaro Caballero,[d] Mario J. Muñoz-Batista,[a,e*] and Rafael Luque[a,f*]

[a] Departamento de Química Orgánica, Universidad de Córdoba, Campus de Rabanales, Edificio Marie Curie (C-3), Ctra Nnal IV-A, Km 396, E14014, Cordoba, Spain.

[b] Department of Chemistry, University of Texas at El Paso, 500 W. University Avenue, El Paso, Texas 79968, United States.

[c] Departamento de Química Física y Termodinámica Aplicada, Instituto Universitario de Nanoquímica (IUNAN), Facultad de Ciencias, Universidad de Córdoba, Campus de Rabanales, Ed. Marie Curie, E-14071 Córdoba, Spain.

[d] Departamento de Química Inorgánica e Ingeniería Química, Instituto Universitario de Investigación en Química Fina y Nanoquímica IUIQFN, Facultad de Ciencias, Universidad de Córdoba, Campus de Rabanales, Ed. Marie Curie, E-14071 Córdoba, Spain.

[e] Department of Chemical Engineering, Faculty of Sciences, University of Granada. Avda. Fuentenueva, s/n 18071, Granada, Spain.

[f] Peoples Friendship University of Russia (RUDN University), 6 Miklukho-Maklaya Str., 117198, Moscow, Russia.

*M.J.M-B. jmunoz385x@gmail.com, *R.L. rafael.luque@uco.es

¥ These authors contribute equally to this work.

Abstract

A graphitic carbon nitride nanostructure has been successfully functionalized by incorporation of different silver contents and subsequent modification with an α-rich protein, namely hemoglobin. Mechanochemistry has been employed, as an efficient and sustainable procedure, for the incorporation of the protein. A complete characterization analysis has been performed following a multitechnique approach. Particularly, XPS data exhibited considerable differences in the C1s region for the Hb/xAg@CN, ensuring the successful protein anchorage on the surface of the graphitic carbon nitride-based materials. The as-synthesized nanomaterials delivered impressive performance towards hydrogen evolution reactions with an overpotential of 79 mV at a current density of 10 mA/cm^2 for Hb/20Ag@CN nanohybrids, which is comparable with the most efficient HER electrocatalysts reported in the literature. The outstanding HER properties were associated with the unique synergistic interactions, quantitatively measured, between AgNPs, Hb tertiary architecture and the graphitic carbon nitride networks.

Keywords: Mechanochemistry, graphitic carbon nitride, silver nanoparticles, hemoglobin, bioconjugates, hydrogen evolution reaction, electrocatalysis, synergy.

Introduction

Development of cost-effective and more sustainable alternatives for efficient electrochemical water splitting reactions is becoming a cornerstone to construct cheaper renewable energy technologies, such as hydrogen fuels cells, with both high electrocatalytic yields and stabilities.[1,2] Among the water-splitting reactions lead by an electrochemical control, hydrogen evolution reactions (HER) constitute a fundamental step and, in turn, have been widely explored to shed light on the mechanistic knowledge of electrocatalytic processes. Up to now, Pt supported onto

carbon based-nanomaterials has delivered outstanding HER electrocatalytic properties such as very high current densities and tiny Tafel slopes.[3,4] Despite their high efficiency, Pt-based catalysts still maintaining several drawbacks for HER practical applications including low durability, very expensive prices and poor scale up. In this way, a number of endeavours has been performed towards the partial or total replacement of Pt for other less inexpensive transition metals such as Ag, Ni, Co, Fe and Cu to gain a more sustainable electrocatalytic hydrogen generation.[5–10] However, transition metals usually undergo significant corrosion when they are exposed to acidic environment, which clearly limit their practical applications.[11]

Recently, some works have been focused on the use of graphitic carbon nitride (g-C_3N_4, CN) based composites to create highly efficient HER electrocatalytic frameworks as a successful approach to replace partially,[12–14] or even totally[14,15] metal-based counterparts and in turn avoid corrosion processes. Although it is well-known that CN exhibit poor electrocatalytic responses owed to its low conductivity and in some cases low surface area, very innovative strategies have been used to greatly improved its HER performance.

For instance, hydrothermal carbonization,[16] encapsulation of nanoparticles,[17] design of C_3N_4 quantum dots on graphene nanoplatforms[18] or even hybrid CN-graphene nanostructures in which carbon nitride provides highly active HER sites and graphene assures fast electron transfer towards the proton reduction, have achieved very outstanding performances towards electrocatalytic hydrogen evolution reactions.[19] Interestingly, it should be highlighted that exceptional electrocatalytic HER performances have been reached by the strong synergistic effects between porous CN nanolayers and N-doped graphene into three dimensional (3D) g-C_3N_4@GO films.[20] The synergistic coupling effect between the large number of catalytically active defects and edges of CN network with both the hierarchically structured film and the excellent conductive properties

of graphene layers, have markedly boosted the electrocatalytic yields of C_3N_4 nanosheets. In the same way, a superb HER electrocatalytic behaviour was observed by the synergistic connection between well-dispersed MoO_2 nanoparticles and P-doped carbon in MoO_2@PCRGO heterostructures.[21] Importantly, the higher HER performance was achieved through the synergistic effect between the single Pt atoms embedded in the pyridinic N_2C_2 defect sites of the melamine-derived graphitic tubes that encapsulated a FeCo metal clusters and copper inside tube walls.[22] Therefore, the hybridization of catalytically active components with other N-doped carbon-based materials seems to be, up to now, an unbeatable strategy to construct highly efficient hydrogen evolution electrocatalysts.

Hemoglobin (Hb) is a tetrameric redox protein formed by four polypeptide chains in which each polypeptide domain encloses at least one iron active redox center. It can provide a hierarchically structured and porous framework which is able to react to environmental stimulies[23] and therefore could acts like as intelligent platforms towards the oxygen adsorption processes.

In this work, we have mechanochemically synthesized two carbon nitride based nanomaterials composed of AgNPs, Hb and CN for hydrogen evolution reactions. The HER performances of both nanobiomaterials were compared with the bi-component precursors 10Ag@CN, 20Ag@CN and Hb/CN, being by far the most efficient catalytically active materials. The latter electrocatalytic trend is associated with the significant synergistic connection of AgNPs, Hb tertiary structure and g-C_3N_4 porous networks reached after the mechanochemical synthetic procedure.

Experimental

Synthesis of materials

g-C_3N_4 (CN) was prepared following previously reported protocol.[24] 5 g of melamine (Sigma-Aldrich) was calcined in a semi-closed system (alumina crucible with a cover) at 580 °C for 2 h

using a heating rate of 5 °C min^{-1}. Ag@CN samples were obtained by a simple chemical reduction method. In a typical experiment, a solution $AgNO_3$ (0.5 M) is added to a previously prepared suspension of the CN support in ethylene glycol. After 1 h under sonication, the adequate amount ($Ag/NaBH_4$ molar ratio 1/7) of a $NaBH_4$ aqueous solution (0.1 M) was quickly added into the mixture under continuous vigorous stirring. The final solid was filtered and profusely rinsed with distilled water and acetone. The obtained Ag@CN samples, as well as CN (450 mg), were modified with Hb, following a mechanochemical protocol at 200 rpm for 10 min. (Retsch PM100 ball mill, 125 mL reaction chamber and eighteen 10 mm stainless steel balls), using 50 mg of Hb in 300 µL of NaH_2PO_4 buffer (pH=7). The nomenclature used to identify the materials is: Hb/xAg@CN where x is the wt.% of Ag (10 or 20, respectively).

Characterization of materials

XRD analysis was performed in the Bruker D8 Advance Diffractometer with the LynxEye detector. The XRD patterns were recorded in a 2θ scan range from 10° to 70°. Bruker Diffrac-plus Eva software, supported by Power Diffraction File database, was used for phase identification. N_2 adsorption-desorption measurements were performed in the Micromeritics ASAP 2000 equipment. The samples were previously degassed for 24 h under vacuum ($p<10^{-2}$ Pa). In addition, SEM-EDX images were acquired in the JEOL-SEM JSM-7800 LV scanning microscope.

XPS experiments were accomplished in an ultrahigh vacuum multipurpose surface analysis instrument SpecsTM. The samples were evacuated overnight under vacuum (10^{-6} Torr) and subsequently, measurements were performed at room temperature using a conventional X-ray source with a Phoibos 150-MCD energy detector. XPS spectra were analyzed employing the XPS CASA software.

FTIR spectra were recorded on an infrared spectrophotometer (ABB MB3000 with Horizon MBTM software) equipped with an ATR PIKE MIRacleTM sampler and a window of ZnSe, and 256 scans were acquired at a resolution of 8 cm^{-1}. During the measurements, the sample was purged with a dehydrated and deoxygenated nitrogen flow (20 mL min_1). The spectra were recorded at room temperature in the 4000–600 cm_1 wavenumber range.

The UV-vis analysis was carried out in the LAMBDA 365 UV/Vis Spectrophotometer, using an integrating sphere and solid sample accessories. UV-vis spectra were obtained in a 200-800 cm^{-1} wavelength range, employing the UV-Express software.

Preparation of the electrodes

Prior to coating, 10x10 mm ITO glasses were washed following a standard procedure. Firstly, the glasses were washed with distilled water and soap. Sequentially, the electrodes were washed in an US bath with deionized water, ethanol and acetone. Sample/ITO electrodes were prepared by dispersing 1 mg of each different sample into 1 ml of ethanol and by drop casting the mixture (90 µL) over ITO surfaces.

Electrochemical methods

Linear-sweep voltammetry measurements (LSV) were performed in a three-electrode electrochemical cell Potentiostat/Galvanostat Autolab (Solartron1286). 50 mL of a 0.5 M aqueous solution of H_2SO_4 was employed as electrolyte. Ag/AgCl was used as the reference electrode; a Pt substrate was used as counter electrode and the different Hb/xAg@CN and xAg@CN/ITO electrodes as working electrodes. It should be pointed out that the area of the Pt substrate was at least ten times higher than the geometrical WE areas with the objective to avoid the deposition of Pt nanodots on the CN-based materials through the formation of large energy barrier.[25] A glassy carbon disc of 5 mm in diameter (Pine Instruments Company) was used as working electrode for

the rotating disc electrode (RDE) measurements. All electrochemical experiments were performed employing a potential range from 0.00 V to -0.75 V vs Ag/AgCl at a scan rate of 2 mV/s. All potentials were referenced to RHE by adding a value of (0.205 + 0.059 x pH) V.

To calculate the faradaic efficiency (FE) for HER of the best electrocatalyst, chronoamperometry measurements at a constant potential (E = - 150 mV) for two specific times were carried out, and the volumes of the generated hydrogen were measured by water displacement method. Then, FE values were estimated by comparing the experimental volume of produced hydrogen with the theoretically calculated for the charge passed (e. g. considering a conversion of 100 %, 1 C should produce 0.116 mL of H_2), using the following equation:

$$FE = 2F \cdot \frac{n_{H_2}}{Q}$$

Where n_{H2}(mol) is the total amount of hydrogen produced and Q(C) is the total amount of charge passed through the cell. Two different durability tests were carried out: On the one hand, chronopotenciometric measurements at a current density of - 10 $mA \cdot cm^{-2}$ for 12 h were recorded. And, on the other hand, the initial current density was monitored at a constant potential of -0.15 V during 600 cronoamperometric cycles.

Results and discussion

Through this work, protein modified xAg@CN nanomaterials have been prepared employing a highly sustainable and efficient procedure, previously reported by our group.[26–29] Namely, the synthesis has been developed by a simple and reproducible mechanochemical methodology (Scheme 1). Such approach has been employed by our group to the synthesis of bioconjugates, composed of metal oxide nanoparticles and several proteins. Remarkably, it has been reported that

proteins with high α-helix content, such as Hb, retained their native-like properties after the mechanochemical synthesis.

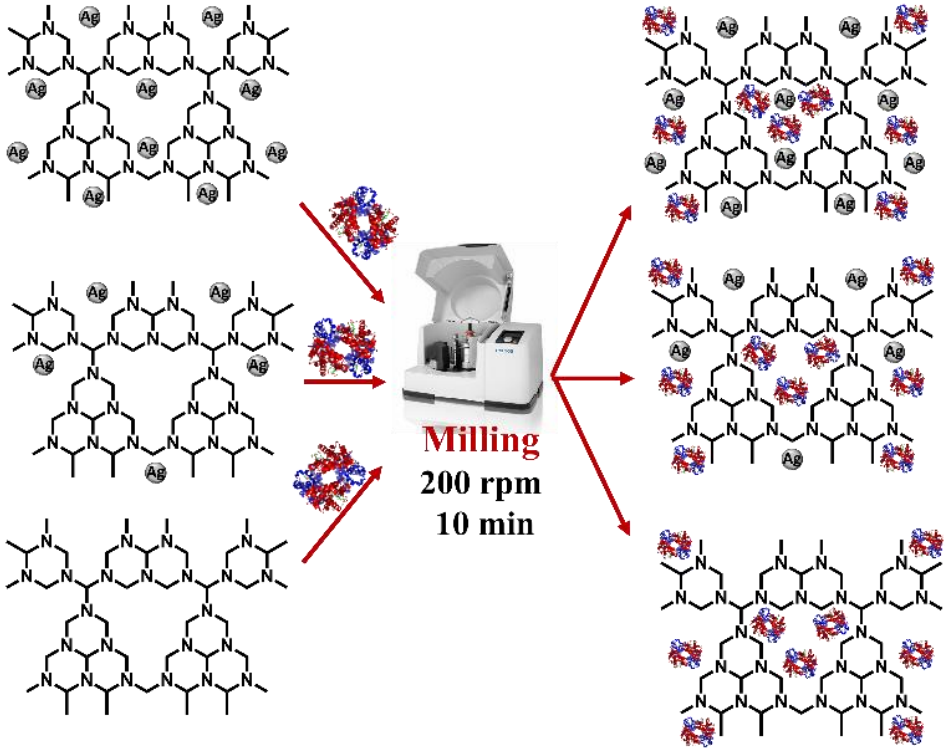

Scheme 1. Illustrative representation of the synthetic strategy of Hb/xAg@CN.

The structure and arrangement of the synthesized carbon nitride material, as well as the post-modified samples, were analysed by X-ray diffraction. As shown in the XRD patterns (Figure 1), all the samples exhibited the typical interlayer-stacking (002) reflection of disordered carbon in a graphitic CN layered structure.[30–34] In addition, a peak around 13.1° can be observed in the diffraction patterns, which could be associated with the (100) reflection.[30–34] The xAg@CN and Hb/xAg@CN samples showed additional peaks at of 38.1°, 44.3° and 64.3° related to (111), (200) and (220) crystallographic planes of metallic silver.[30,35]

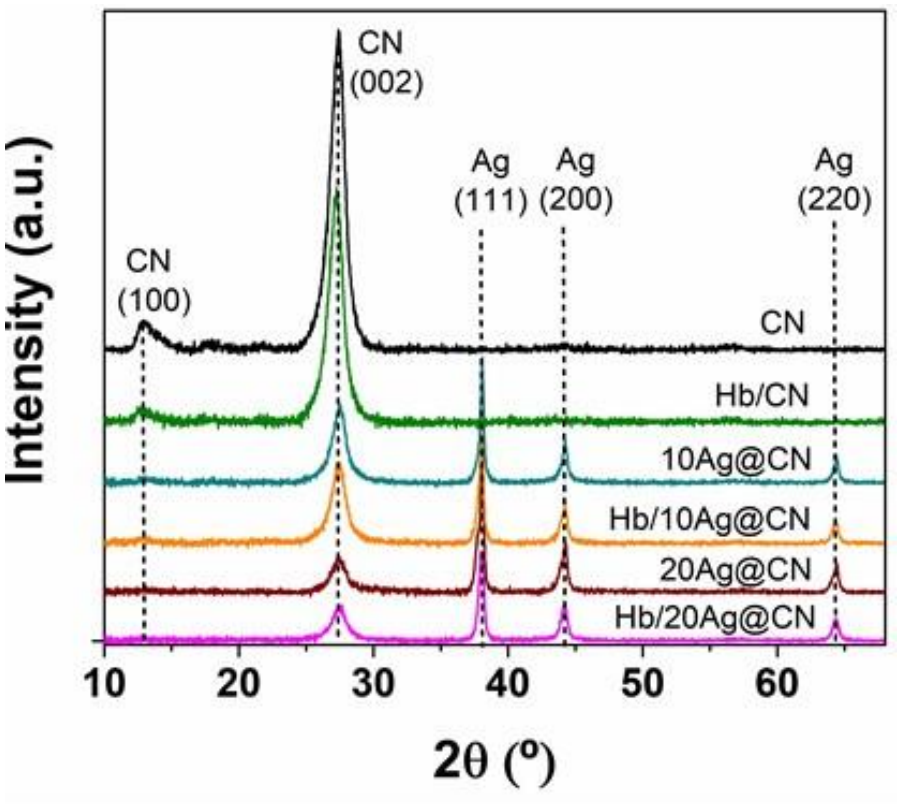

Figure 1. XRD patterns of prepared samples.

Morphological properties of samples and references obtained by N_2 physisorption are presented in Table 1 and Figure S1. In this table, it is shown that the CN support (reference) presents the higher surface area in comparison with Ag@CN samples. In fact, a decreasing trend can be highlighted with the amount of silver, which indicates that silver particles could be blocking some porous of the CN structure. Less influence seems to has the incorporation of Hb on the surface of Ag-modified materials with negligible variation most likely related to the experimental error. In any case, the small differences detected after functionalization with both Ag and Hb, strongly suggest that this observable is dominated by the major CN component. The same conclusion can be deduced from pore volume and pore size data (Table 1).

Table 1. Morphological properties of the samples.

Sample	Area BET (m^2/g)	Pore volume (cm^3/g)	Pore size (nm)
10Ag@CN	19.1	0.092	18.5
20Ag@CN	18.5	0.091	18.6
Hb/10Ag@CN	18.6	0.090	18.5
Hb/20Ag@CN	17.8	0.089	18.4
Hb/CN	24.8	0.096	19.8
CN	25.1	0.099	20.1

The effective deposition of silver entities on the CN surface was evidenced by SEM-mapping results (Figure 2, SEM-mapping of 20Ag@CN and Hb/20Ag@CN). This analysis revealed the presence of carbon, nitrogen, oxygen, and silver. Although some silver agglomeration can be appreciated in certain regions of the sample, it could be said that all the elements are homogeneously distributed on the materials surface. Interestingly, in the hemoglobin modified samples, certain iron content can be appreciated, suggesting the effectiveness of the protein functionalization process. In addition, TEM image and particle size distribution of Hb/20Ag@CN material, as representative sample, can be seen in Figure S2. A mean radius of 9.5 nm was found for silver nanoparticles with quasi-spherical morphology.

Figure 3 displays the FT-IR of the six prepared samples. The obtained spectra showed carbon nitride-like fingerprints for all the materials, suggesting that the CN component retained its main structural characteristics after the incorporation of both, metal and protein counterpart. Specifically, the bands observed around 3500–2500 cm^{-1} could be mainly associated with N-H stretching vibration contributions of residual NHx groups in CN structure. Nonetheless, the

presence of amino groups from Hb, in the protein modified materials, and adsorbed water molecules may also need to be taken into account.[24,36] As well, in the 1600–1000 cm^{-1} region, several contributions can be visualized most likely assigned to N-C stretching modes of heterocycles from the CN structure. The characteristic amide I and II bands of proteins, normally observed around 1650-1500 cm^{-1}, were found overlapped by CN bands, in the three protein-modified materials. The amide I band signal is characteristic from C=O stretching vibrations of peptide linkages, while amide II band resulted from a combination of N–H in plane bending and C–N stretching vibrations of the peptide groups. Nonetheless, not clear evidence of the protein functionalization can be exposed from this analysis. Furthermore, around 804 cm^{-1} was observed a clear and distinguish peak, associated with the breathing modes of tris-s-triazine (C_6N_7-based) building blocks.[37,38]

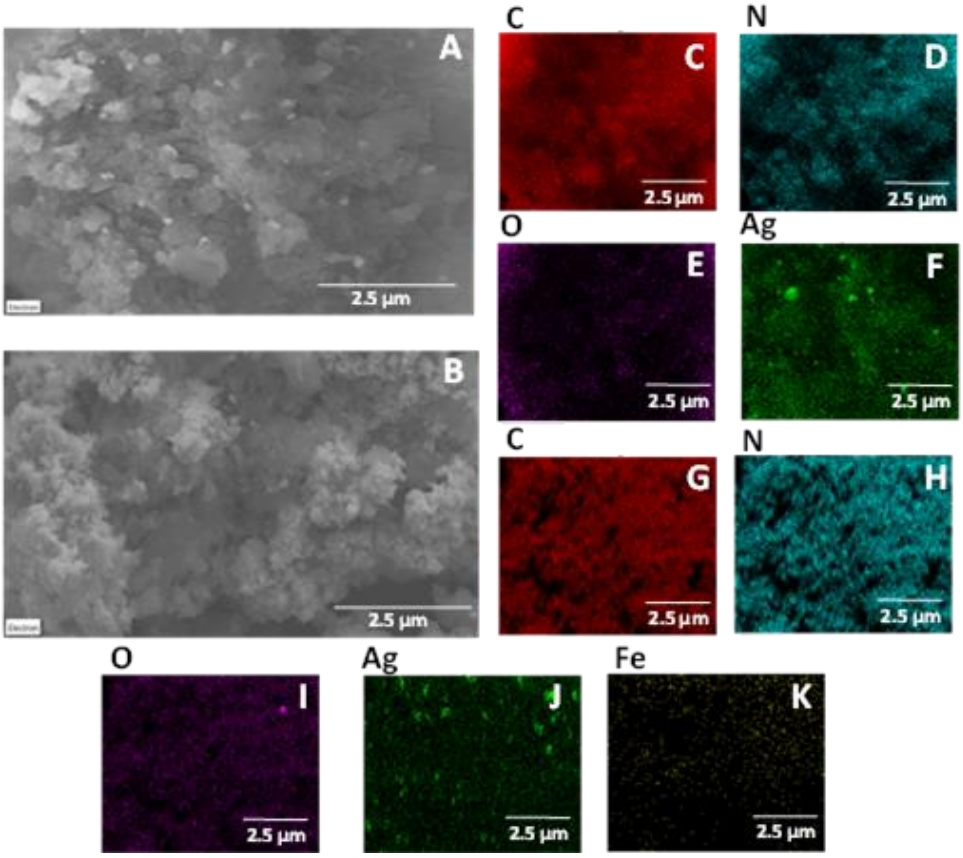

Figure 2. SEM micrographs of (A) 20Ag@CN and (B) Hb/20Ag@CN, respectively. (C-F) SEM-mapping images of 20Ag@CN and (G-K) EDX-mapping images of Hb/20Ag@CN.

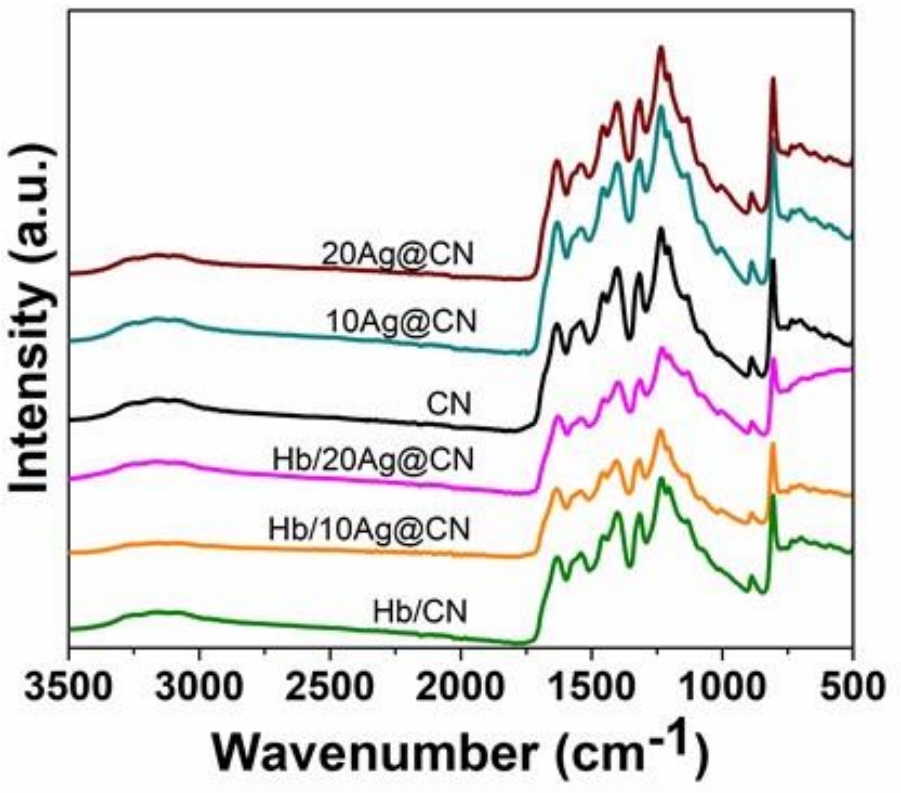

Figure 3. FT-IR spectra of prepared samples.

Chemical properties of the samples were also studied by XPS measurements. Carbon 1s (C1s), Nitrogen 1s (N1s) and Silver 3d (Ag 3d) XPS regions of designed samples were measured as can be seen in Figure 4A, B and C, respectively. Importantly, very marked differences were detected in C1s region before and after the incorporation of Hemoglobin (Figure 4A). While 20Ag@CN and 10Ag@CN showed very similar spectrum, a clear intensity enhancement was detected for samples, Hb/20Ag@CN, Hb/10Ag@CN and Hb/CN in C-C contribution situated at 284,6 eV (Figure 4D). In addition, as previously reported in similar systems, detected C-O contribution can be exclusively ascribable to Hemoglobin protein.[27] Remaining peaks considered during the fitting

of Figure 4D can be associated with both carbon nitride structural moieties, e.g., bridging carbons between aromatic moieties (C3−N: 286.2 eV) or at the aromatic rings (N−C−N; 287.8 eV) as well as C-N from the protein chain.[24,27] For N1s XPS region, the fitting considered the last C-N mentioned species as well as the contribution from N-H moieties and the broad π excitation usually reported in g-C_3N_4-based materials.[39] C1s and N1s spectra supported data obtained by FT-IR, indicating that rather minor differences in terms of the carbon nitride component are generated by incorporation of silver nanoparticles. Additionally, the introduction of Hb modifies the final XPS spectra (C1s and N1s) by overlapping contributions, without considerable structural distortion of the major CN component. Finally, Ag 3d XPS region showed two contributions that are indicative of the metallic state of the noble metal in all synthesised materials (Figure 4F). [30,40]

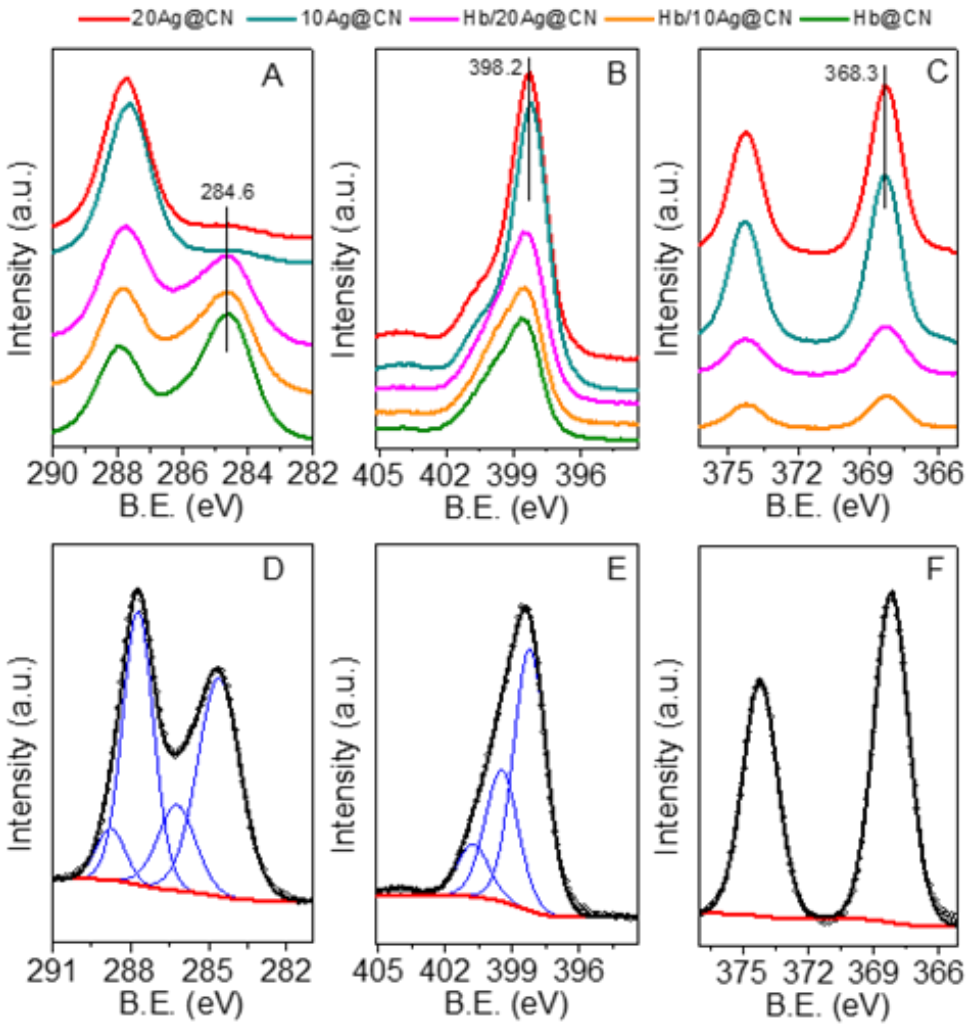

Figure 4. XPS spectra of the prepared samples in the (A) C1s, (B) N1s and (C) Ag3d regions. Deconvoluted XPS spectra of Hb/20Ag@CN for (D) C1s, (E) N1s and (F) Ag 3d.

With the aim to explore and compare the electrocatalytic behaviour towards HER reaction of Hb/10Ag@CN and Hb/20Ag@CN electrodes with respect to the activities of bi-component CN based compounds (10Ag@CN, 20Ag@CN, Hb/CN), a set of linear sweep voltammetry experiments (LSV) were performed in 0.5 M of H_2SO_4 at a scan rate of 2 mV/s on a three-electrode cell (Figure 5A). It should be highlighted that the current densities of Figure 5A were calculated from the electrochemical surface area of the electrocatalyst following a method reported in

previous works.[5,41] Noteworthy, the current density values produced by the two-component precursors (10Ag@CN and 20Ag@CN) were 22 mA cm^{-2} and 32 mA cm^{-2} at -0.6 V, respectively, while this parameter underwent a striking enhancement to 96 mA cm^{-2}, 140 mA cm^{-2} and 180 mA cm^{-2}, upon the addition of protein platforms, for the Hb/CN, Hb/10Ag@CN and Hb/20Ag@CN composites, respectively. The HER activity of the composites was further compared taking in account the needed overpotentials to achieve a current density of 10mA cm^{-2}, which represent a very important parameter to know the efficiency of the HER electrocatalytic processes. As can be observed in Figure 5A the overpotential values were -280 mV, -213 mV, -132 mV, -104 mV and -79 mV vs RHE for the 10Ag@CN, 20Ag@CN, Hb/CN, Hb/10Ag@CN and Hb/20Ag@CN, respectively. It should be pointed out the shift of the overpotentials to less negative values at a fixed density current is a clear signal of the improvement of the electrocatalytic efficiency of HER reactions. Therefore, the three-component heterostructures HER activity surpassed by far the catalytic properties of the bi-component composites, which has demonstrated that the integration of AgNPs, Hb and CN networks in a synergistic fashion is able to produce HER electrocatalytic materials with higher performances. Remarkably, Hb/20Ag@CN beat in terms of overpotential to most of the CN based materials reported, up to now, in the literature (Figure 5D).

The evaluation of the Tafel slopes is usually used to elucidate the HER mechanistic pathways. Figure 5C displays the Tafel slopes for both, the three-component hybrids Hb/10Ag@CN, Hb/20Ag@CN composites and the bi-component composites 10Ag@CN, 20Ag@CN, Hb/CN. As is expected, the Tafel slope obtained for Hb/20Ag@CN (155mV/dec) exhibits a comparatively lower value to those obtained for the other composites, suggesting the most HER proficient

kinetics among all composites, which is reached by the synergistic integration of well-dispersed AgNPs 20% wt, Hb architectures and CN surfaces.

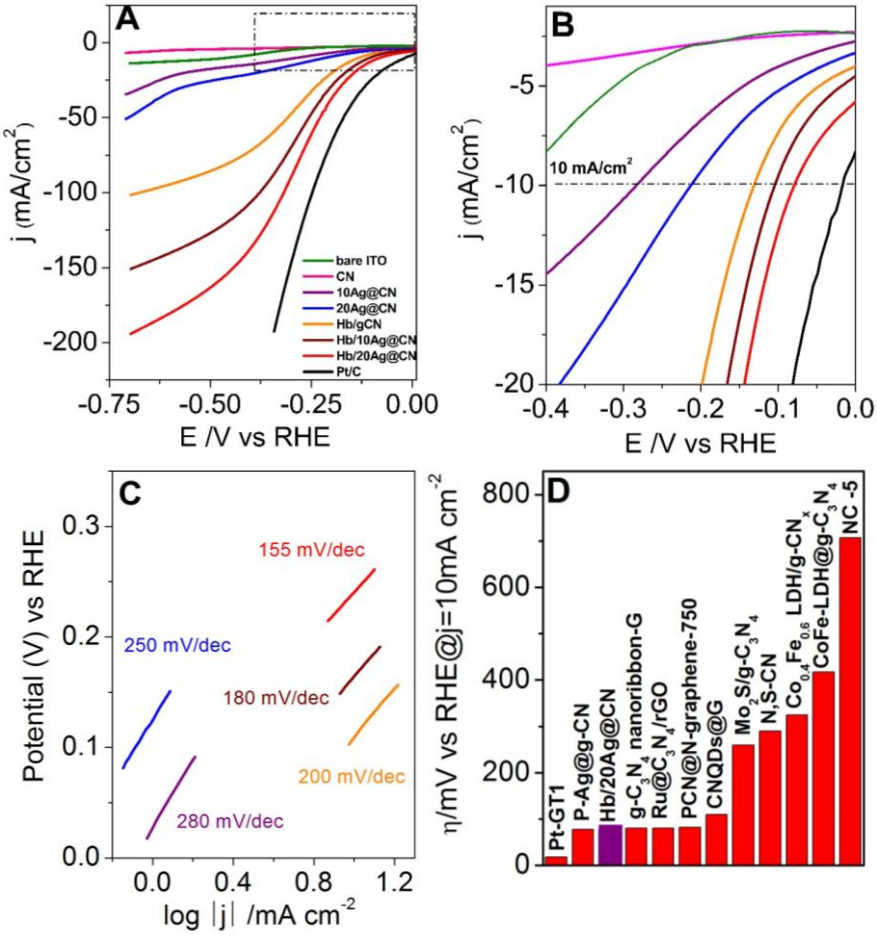

Figure 5. (A) LSV for HER reaction of Ag10@gC_3N_4, Ag20@gC_3N_4, Hb@gC_3N_4, Hb@Ag10gC_3N_4, Hb@Ag20gC_3N_4 and commercial Pt/C at a scan rate of 2mV/s. (B) Amplified curves, (C) Tafel plots of Ag10@gC_3N_4, Ag20@gC_3N_4, Hb@gC_3N_4, Hb@Ag10gC_3N_4 and Hb@Ag20gC_3N_4 nanocomposites and (D) Comparison of Hb/20Ag@CN with CN-based materials reported (η@j=10 mA cm^{-2}). Pt-GT1:[22] P-Ag@gCN.[42] g-C_3N_4 nanoribbon-G.[43] CNQDs@G.[18] Ru@C_3N_4/rGO.[44] PCN@N-graphene-750.[20] Mo_2S/g-C3N4.[45] N,S-CN.[46] $Co_{0.4}Fe_{0.5}$LDH/g-CNx.[47] CoFe-LDH@g-C_3N4.[48] NC-5. [49]

The proposed mechanism for HER processes in acidic medium consists of two steps (i) the Volmer step, (ii) the desorption step or Heyrovsky process and (iii) the recombination step or Tafel step.

(i) $Hb/20Ag@CN + H_3O^+ + e- = Hb/20Ag@CN\text{-}H_{ab}$

(ii) $Hb/20Ag@CN\text{-}H_{ab} + e- + H_3O^+ = Hb/20Ag@CN + H_2 + H_2O$

(iii) $Hb/20Ag@CN\text{ -Hab} + Hb/20Ag@CN\text{ -Hab} = H_2 + Hb/20Ag@CN$

To identify the limiting stage in the HER process for the Hb/20Ag@CN nanocomposite, RDE voltammetry measurements from 0 to 2500 rpm of rotation rate were carried out (Figure 6A). The hydrogen evolution rate increases significatively with the rotation rate, further confirming both that the mass diffusion of proton is limiting stage, and the Heyrovsky step may be the rate-determining step (RDS).[50,51] In addition, this experiment clearly confirms that H_2 evolution is not produced from the decomposition of Hb.

The faradaic efficiency for HER of the Hb/20Ag@CN nanocomposite was calculated by comparing the theorical volume of produced hydrogen with the experimentally measured (see experimental section). The resulting faradaic yield was 0.94 over 1, a value very near to the maximum possible one (Figure 6B). The TON of the electrocatalyst was $3.9x10^4$ using 1 mg of catalyst, which is comparable with other data reported in the literature for HER reactions.[52] In addition, the durability of Hb/20Ag@CN was firstly tested at a constant current density of 10 $mA \cdot cm^{-2}$ for 12 h. As it can be observed in Figure 6C, the potential remained almost constant during this time course. Secondly, Figure 6D shows that the percentage of the initial current density was maintained almost constant after 600 cycles. Therefore, both durability tests demonstrate the good electrochemical stability of the Hb/20Ag@CN nanocomposite.

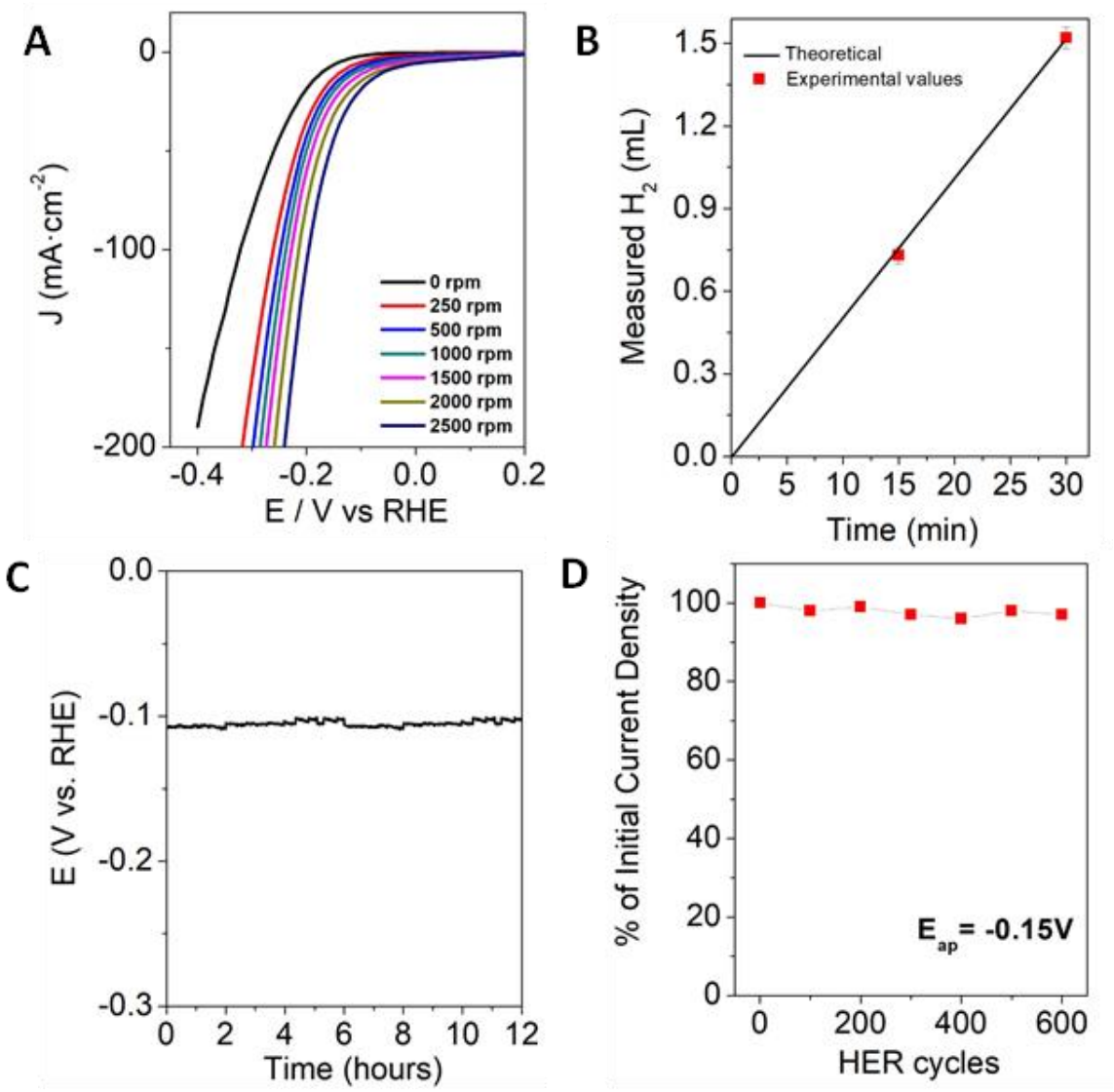

Figure 6. (A) RDE voltammograms of GC electrode modified with Hb/20Ag@CN at different rotating rates. Scan rate: 2 $mV \cdot s^{-1}$. (B) Faradaic efficiency plots for HER (calculated versus experimental hydrogen production at a constant potential). (C, D) Long-term stability studies: (C) Chronopotentiometric measurement at 10 $mA \cdot cm^{-1}$ for 12 h, and (D) Monitoring percentage of initial current density after 600 chronoamperometric cycles at a constant potential of -0.15 V.

In order to quantify the effect of the components to the electrochemical responses, a simple function of the ternary system (Hb-Ag-CN) can be defined with respect to the major component (CN) and the parent binary counterpart (Equation 1).[24,53]

$$\boldsymbol{j}(\text{Hb/xAg@CN; } \mathbf{theoretical}) = \boldsymbol{j}(\text{CN}) + \nabla\left(\boldsymbol{J}(\text{Ag@CN, real}) - \mathbf{j}(\text{CN})\right) + \nabla\left(\boldsymbol{j}(\text{Hb/CN}) - \boldsymbol{j}(\text{CN})\right) \quad (1)$$

Equation 1 allows to determine if the interaction between the surface species present in the Hb/xAg@CN samples is detrimental, additive or, as desired, synergistic. The difference between the electrochemical response of Hb/xAg@CN, theoretical and real, could be negative, zero or positive. In Figure 7, the sum described by Eq. 1 is presented next to the real measured for Hb/xAg@CN. The corresponding differences are included as numerical values in the plots. The graphical analysis confirms that a synergistic effect occurs and would correspond to ca. 12 and 24 % for Hb/10Ag@CN and Hb/20Ag@CN, respectively. It is well-known that the defects and edges of CN are effective catalytic sites for HER owed to they favour the water splitting processes ($2H_2O=2H_2 + O_2$).[11] In this direction, 3D nanostructured protein networks provide a porous framework in which the synergistic interactions between their components give rise to a large number of nitrogen structural defects that strongly increase the adsorption of hydronium ions and therefore the HER performances. Additionally, it was appreciated a clear extra-improvement of the HER with higher silver content. It can be explained considering the influence of the well-distributed AgNPs pattern on the Hb/CN platforms, which contribute to boost the HER efficiency through the increment of the number of efficient electrocatalytically active centers at the electrochemical interfaces.

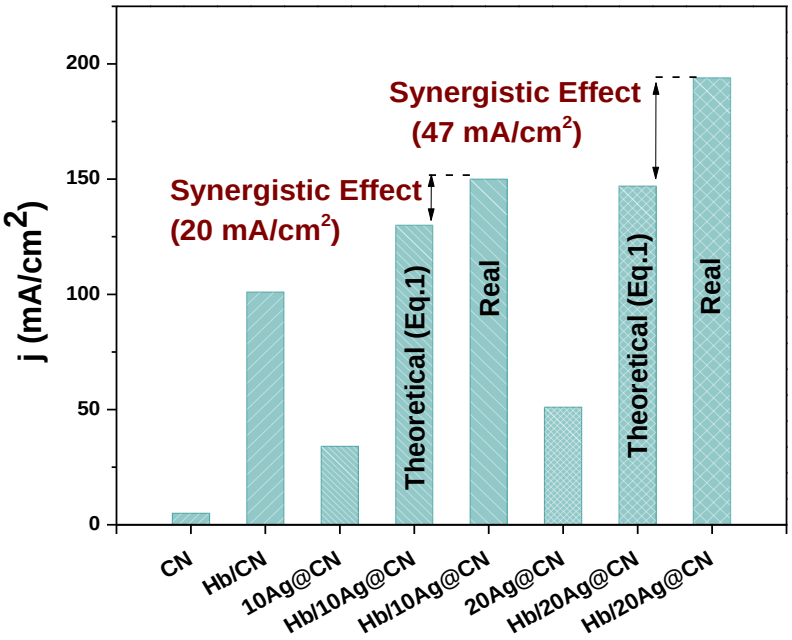

Figure 7. Current density. Illustrative representation of synergistic effect.

As well post-characterization of the material was performed by UV-vis and XPS techniques. XPS analysis was performed for both spent and fresh Hb/20Ag@C_3N_4 material. C1s XPS regions (Figure S3A) exhibited four contributions in both materials, before and after the electrochemical reaction, associated with C-C (284.6 eV in both cases), C_3−N mainly from carbon nitride structural moieties (286.3 eV in both cases), N−C−N from the protein chain or from the aromatic rings of C_3N_4 structure (287.8 and 288.3 eV for fresh and spent sample, respectively), and C-O mainly from the protein entities (288.8 and 289.3 eV for fresh and spent sample, respectively). The latest two signal, related to N-C-N and C-O bonds shifted 0.5 eV, which could be associated with slight changes in the native-like structure of the protein. Nonetheless, the presence of four carbon contributions in similar positions for the fresh and spent materials, indicated that the material does not suffer considerable modifications after the electrochemical reaction. It is also worth to remark that after immobilization of the material in the ITO, the increment in the intensity of the C-C signal could be understood by the additional contribution of C from

the ITO support. Figure S3B displayed N1s XPS spectra of fresh and spent sample, which could be deconvoluted in three main peaks, with no considerable variation. Importantly, Ag 3d spectrum of both samples exhibited negligible differences, therefore confirming that silver was not oxidized during the electrochemical reaction and in turn it was found as metallic silver after the test (Figure S3C). In addition, to get more insights into the chemical changes in the porphyrin environment, XPS analysis was performed in the Fe2p region (Figure S4). The observed low intensity was associated with the low iron content in the samples, which hinder the deep analysis of this XPS region. Nonetheless, it can be clearly observed that $Fe2p_{3/2}$ was located at 710.9 eV, being attributed to iron oxidized species.

Additionally, UV-vis measurements were performed for the Hb/20Ag@C_3N_4 material, before and after the electrochemical reaction (Figure S5). As well, pure hemoglobin was treated under the same conditions and UV spectra of both samples was obtained. Hb/20Ag@C_3N_4 spectra showed a blue shift, in comparison with the free protein, which could be associated with slight modifications in the secondary structure of the protein after the synthetic protocol. However, no considerable changes were observed after the electrochemical reaction. In turn, after treating free hemoglobin in the same reaction conditions, a clear shift of the UV band was observed. Such results indicated that even if after the synthetic protocol certain changes occurred in the Hb structure, immobilization strategy clearly confers a good stability to the protein for being used in the electrochemical tests. It is well-known that the conformational changes of enzymes can significantly improve their electrocatalytic behaviour.[29] In our work, the slight modifications of the 3D hemoglobin structure is probably increasing the number of N catalytically active sites in the bioconjugate heterostructures which directly contribute to the HER improvement.

Conclusions

A sustainable mechanochemical approach has been successfully employed for the preparation of biohybrid materials composed of graphitic carbonitrile, silver nanoparticles and an α-rich protein, namely hemoglobin. Electrochemical hydrogen evolution of silver modified graphitic carbonitrile materials was enhanced through a synergistic effect by the incorporation of hemoglobin. Protein networks on the surface of CN materials could give rise to nitrogen structural defects, which may facilitate adsorption of hydronium ions and therefore improve the HER performances. As well, higher silver content on the materials resulted in a better HER efficiency, which could be associated with the increment of electrocatalytically active centers at the electrochemical interfaces. Therefore, the as-synthesized CN-based materials could be potentially used for the development of proficient and sustainable hydrogen fuels cells.

Conflicts of interest

There are no conflicts to declare.

Acknowledgements

Rafael Luque gratefully acknowledges MINECO for funding project CTQ2016-78289-P, co-financed with FEDER funds. Daily Rodriguez-Padron and Alain R. Puente-Santiago also gratefully acknowledges MINECO for providing research contract under the same project. M. C. thanks the “Plan Propio de Investigación” from the Universidad de Córdoba (UCO) and the “Programa Operativo de fondos FEDER Andalucía” for its financial support

through a postdoctoral contract (Modality 5.2.A). M. J. Muñoz-Batista acknowledges MINECO for a Juan de la Cierva postdoctoral contract (ref. FJCI-2016-29014). RUDN University Program 5-100 has contributed to the preparation of this work.

References

(1) Luo, J.; Im, J.-H.; Mayer, M. T.; Schreier, M.; Nazeeruddin, M. K.; Park, N.-G.; Tilley, S. D.; Fan, H. J.; Grätzel, M. Water Photolysis at 12.3% Efficiency via Perovskite Photovoltaics and Earth-Abundant Catalysts. *Science* **2014**, *345,* (6204), 1593–1596. DOI: 10.1126/science.1258307.

(2) Tilley, S. D. Recent Advances and Emerging Trends in Photo-Electrochemical Solar Energy Conversion. *Adv. Energy Mater.* **2019**, *9* (2), 1802877. DOI: 10.1002/AENM.201802877.

(3) Zhang, H.; An, P.; Zhou, W.; Guan, B. Y.; Zhang, P.; Dong, J.; Lou, X. W. (David). Dynamic Traction of Lattice-Confined Platinum Atoms into Mesoporous Carbon Matrix for Hydrogen Evolution Reaction. *Sci. Adv.* **2018**, *4* (1), eaao6657. DOI: 10.1126/sciadv.aao6657.

(4) Feng, J.-X.; Tong, S.-Y.; Tong, Y.-X.; Li, G.-R. Pt-like Hydrogen Evolution Electrocatalysis on PANI/CoP Hybrid Nanowires by Weakening the Shackles of Hydrogen Ions on the Surfaces of Catalysts. *J. Am. Chem. Soc.* **2018**, *140* (15), 5118–5126. DOI: 10.1021/jacs.7b12968.

(5) Cova, C. M.; Zuliani, A.; Puente Santiago, A. R.; Caballero, A.; Muñoz-Batista, M. J.; Luque, R. Microwave-Assisted Preparation of Ag/AgS2 Carbon Hybrid Structures from Pig Bristles as Efficient HER Catalysts. *J. Mater. Chem. A* **2018**, *6* (43), 21516–21523. DOI: 10.1039/C8TA06417B.

(6) Popczun, E. J.; McKone, J. R.; Read, C. G.; Biacchi, A. J.; Wiltrout, A. M.; Lewis, N. S.; Schaak, R. E. Nanostructured Nickel Phosphide as an Electrocatalyst for the Hydrogen Evolution Reaction. *J. Am. Chem. Soc.* **2013**, *135* (25), 9267–9270. DOI: 10.1021/ja403440e.

(7) Yan, X.; Tian, L.; He, M.; Chen, X. Three-Dimensional Crystalline/Amorphous Co/Co3O4 Core/Shell Nanosheets as Efficient Electrocatalysts for the Hydrogen Evolution Reaction. *Nano Lett.* **2015**, *15* (9), 6015–6021. DOI: 10.1021/acs.nanolett.5b02205.

(8) Son, C. Y.; Kwak, I. H.; Lim, Y. R.; Park, J. FeP and FeP Nanowires for Efficient Electrocatalytic Hydrogen Evolution Reaction. *Chem. Commun.* **2016**, *52* (13), 2819–2822. DOI: 10.1039/C5CC09832G.

(9) Ren, H.; Xu, W.; Zhu, S.; Cui, Z.; Yang, X.; Inoue, A. Synthesis and Properties of Nanoporous Ag2S/CuS Catalyst for Hydrogen Evolution Reaction. *Electrochim. Acta* **2016**, *190*, 221–228. DOI: DOI: 10.1016/J.ELECTACTA.2015.12.096.

(10) Farahbakhsh, N.; Sanjabi, S. Activated Cu/Cu2O Foam with Ni Nanoparticles for Electrocatalytic Activity Enhancement of Hydrogen Evolution Reaction (HER) in Acidic Media. *J. Ind. Eng. Chem.* **2019**, *70*, 211–225. DOI: 10.1016/J.JIEC.2018.10.018.

(11) Zheng, Y.; Jiao, Y.; Zhu, Y.; Li, L. H.; Han, Y.; Chen, Y.; Du, A.; Jaroniec, M.; Qiao, S. Z. Hydrogen Evolution by a Metal-Free Electrocatalyst. *Nat. Commun.* **2014**, *5* (1), 3783. DOI: 10.1038/ncomms4783.

(12) Bhowmik, T.; Kundu, M. K.; Barman, S. Palladium Nanoparticle–Graphitic Carbon Nitride Porous Synergistic Catalyst for Hydrogen Evolution/Oxidation Reactions over a Broad Range of PH and Correlation of Its Catalytic Activity with Measured Hydrogen Binding

Energy. *ACS Catal.* **2016**, *6* (3), 1929–1941. DOI: 10.1021/acscatal.5b02485.

(13) Peng, Y.; Lu, B.; Chen, L.; Wang, N.; Lu, J. E.; Ping, Y.; Chen, S. Hydrogen Evolution Reaction Catalyzed by Ruthenium Ion-Complexed Graphitic Carbon Nitride Nanosheets. *J. Mater. Chem. A* **2017**, *5* (34), 18261–18269. DOI: 10.1039/C7TA03826G.

(14) Shinde, S. S.; Sami, A.; Lee, J.-H. Nitrogen- and Phosphorus-Doped Nanoporous Graphene/Graphitic Carbon Nitride Hybrids as Efficient Electrocatalysts for Hydrogen Evolution. *ChemCatChem* **2015**, *7* (23), 3873–3880. DOI: 10.1002/cctc.201500701.

(15) Tan, X.; Tahini, H. A.; Smith, S. C. P-Doped Graphene/Graphitic Carbon Nitride Hybrid Electrocatalysts: Unraveling Charge Transfer Mechanisms for Enhanced Hydrogen Evolution Reaction Performance. *ACS Catal.* **2016**, *6* (10), 7071–7077. DOI: 10.1021/acscatal.6b01951.

(16) Huang, B.; Liu, Y.; Xie, Z. Biomass Derived 2D Carbons via a Hydrothermal Carbonization Method as Efficient Bifunctional ORR/HER Electrocatalysts. *J. Mater. Chem. A* **2017**, *5* (45), 23481–23488. DOI: 10.1039/C7TA08052B.

(17) Wang, Q.; Lei, Y.; Chen, Z.; Wu, N.; Wang, Y.; Wang, B.; Wang, Y. Fe/Fe3C@C Nanoparticles Encapsulated in N-Doped Graphene–CNTs Framework as an Efficient Bifunctional Oxygen Electrocatalyst for Robust Rechargeable Zn–air Batteries. *J. Mater. Chem. A* **2018**, *6* (2), 516–526. DOI: 10.1039/C7TA08423D.

(18) Zhong, H.; Zhang, Q.; Wang, J.; Zhang, X.; Wei, X.; Wu, Z.; Li, K.; Meng, F.; Bao, D.; Yan, J. Engineering Ultrathin C3N4 Quantum Dots on Graphene as a Metal-Free Water Reduction Electrocatalyst. *ACS Catal.* **2018**, *8* (5), 3965–3970. DOI: 10.1021/acscatal.8b00467.

(19) Zhao, Y.; Zhang, J.; Qu, L. Graphitic Carbon Nitride/Graphene Hybrids as New Active Materials for Energy Conversion and Storage. *ChemNanoMat* **2015**, *1* (5), 298–318. DOI: 10.1002/cnma.201500060.

(20) Duan, J.; Chen, S.; Jaroniec, M.; Qiao, S. Z. Porous C3N4 Nanolayers@N-Graphene Films as Catalyst Electrodes for Highly Efficient Hydrogen Evolution. *ACS Nano* **2015**, *9* (1), 931–940. DOI: 10.1021/nn506701x.

(21) Tang, Y.-J.; Gao, M.-R.; Liu, C.-H.; Li, S.-L.; Jiang, H.-L.; Lan, Y.-Q.; Han, M.; Yu, S.-H. Porous Molybdenum-Based Hybrid Catalysts for Highly Efficient Hydrogen Evolution. *Angew. Chemie Int. Ed.* **2015**, *54* (44), 12928–12932. DOI: 10.1002/anie.201505691.

(22) Tiwari, J. N.; Sultan, S.; Myung, C. W.; Yoon, T.; Li, N.; Ha, M.; Harzandi, A. M.; Park, H. J.; Kim, D. Y.; Chandrasekaran, S. S.; Lee, W. G., Vij V., Kang H., Shin T. J., Shin H. S., Lee G., Lee Z. Kim K. S. Multicomponent Electrocatalyst with Ultralow Pt Loading and High Hydrogen Evolution Activity. *Nat. Energy* **2018**, *3* (9), 773–782. DOI: 10.1038/s41560-018-0209-x.

(23) Khairy, M.; El-Safty, S. A. Hemoproteins–nickel Foam Hybrids as Effective Supercapacitors. *Chem. Commun.* **2014**, *50* (11), 1356–1358. DOI: 10.1039/C3CC48155G.

(24) Muñoz-Batista, M. J.; Fontelles-Carceller, O.; Kubacka, A.; Fernández-García, M. Effect of Exfoliation and Surface Deposition of MnOx Species in G-C3N4: Toluene Photo-Degradation under UV and Visible Light. *Appl. Catal. B Environ.* **2017**, *203* (7), 663–672. DOI: 10.1016/j.apcatb.2016.10.044.

(25) Chen, R.; Yang, C.; Cai, W.; Wang, H.-Y.; Miao, J.; Zhang, L.; Chen, S.; Liu, B. Use of Platinum as the Counter Electrode to Study the Activity of Nonprecious Metal Catalysts for

the Hydrogen Evolution Reaction. *ACS Energy Lett.* **2017**, *2* (5), 1070–1075. DOI: 10.1021/acsenergylett.7b00219.

(26) Rodriguez-Padrón, D.; Puente-Santiago, A. R.; Balu, A. M.; Romero, A. A.; Luque, R. Solventless Mechanochemical Preparation of Novel Magnetic Bioconjugates. *Chem. Commun.* **2017**, *53* (54), 7635–7637. DOI: 10.1039/C7CC03975A.

(27) Rodríguez-Padrón, D.; Puente-Santiago, A. R.; Caballero, A.; Benítez, A.; Balu, A. M.; Romero, A. A.; Luque, R. Mechanochemical Design of Hemoglobin-Functionalised Magnetic Nanomaterials for Energy Storage Devices. *J. Mater. Chem. A* **2017**, *5* (31), 16404–16411. DOI: 10.1039/c7ta04135g.

(28) Rodríguez-Padrón, D.; Jodlowski, A. D.; de Miguel, G.; Puente-Santiago, A. R.; Balu, A. M.; Luque, R. Synthesis of Carbon-Based Fluorescent Polymers Driven by Catalytically Active Magnetic Bioconjugates. *Green Chem.* **2018**, *20* (1), 225–229. DOI: 10.1039/C7GC03295A.

(29) Rodríguez-Padrón, D.; Puente-Santiago, A. R.; Caballero, A.; Balu, A. M.; Romero, A. A.; Luque, R. Highly Efficient Direct Oxygen Electro-Reduction by Partially Unfolded Laccases Immobilized on Waste-Derived Magnetically Separable Nanoparticles. *Nanoscale* **2018**, *10* (8), 3961–3968. DOI: 10.1039/C8NR00512E.

(30) Muñoz-Batista, M. J.; Fontelles-Carceller, O.; Ferrer, M.; Fernández-García, M.; Kubacka, A. Disinfection Capability of Ag/g-C3N4 Composite Photocatalysts under UV and Visible Light Illumination. *Appl. Catal. B Environ.* **2016**, *183*, 86–95. DOI: 10.1016/j.apcatb.2015.10.024.

(31) Ong, W.-J.; Tan, L.-L.; Ng, Y. H.; Yong, S.-T.; Chai, S.-P. Graphitic Carbon Nitride (g-C

3 N 4)-Based Photocatalysts for Artificial Photosynthesis and Environmental Remediation: Are We a Step Closer To Achieving Sustainability? *Chem. Rev.* **2016**, *116* (12), 7159–7329. DOI: 10.1021/acs.chemrev.6b00075.

(32) Mamba, G.; Mishra, A. K. Graphitic Carbon Nitride (g-C3N4) Nanocomposites: A New and Exciting Generation of Visible Light Driven Photocatalysts for Environmental Pollution Remediation. *Appl. Catal. B Environ.* **2016**, *198*, 347–377. DOI: 10.1016/j.apcatb.2016.05.052.

(33) Muñoz-Batista, M. J.; Rodríguez-Padrón, D.; Puente-Santiago, A. R.; Kubacka, A.; Luque, R.; Fernández-García, M. Sunlight-Driven Hydrogen Production Using an Annular Flow Photoreactor and g-C3N4-Based Catalysts. *ChemPhotoChem* **2018**, *2*, 870–877. DOI: 10.1002/cptc.201800064.

(34) Caudillo-Flores, U.; Muñoz-Batista, M. J.; Cortés, J. A.; Fernández-García, M.; Kubacka, A. UV and Visible Light Driven H2 Photo-Production Using Nb-Doped TiO2: Comparing Pt and Pd Co-Catalysts. *Mol. Catal.* **2017**, *437*, 1–10. DOI: 10.1016/j.mcat.2017.04.035.

(35) Fontelles-Carceller, O.; Muñoz-Batista, M. J.; Fernández-García, M.; Kubacka, A. Interface Effects in Sunlight-Driven Ag/g-C3N4 Composite Catalysts : Study of the Toluene Photodegradation Quantum Efficiency. *ACS Appl. Mater. Interfaces* **2016**, *8* (4), 2617–2627. DOI: 10.1021/acsami.5b10434.

(36) Yan, H.; Yang, H. TiO2–g-C3N4 Composite Materials for Photocatalytic H2 Evolution under Visible Light Irradiation. *J. Alloys Compd.* **2011**, *509* (4), L26–L29. DOI: 10.1016/J.JALLCOM.2010.09.201.

(37) Zhang, J.; Sun, J.; Maeda, K.; Domen, K.; Liu, P.; Antonietti, M.; Fu, X.; Wang, X. Sulfur-

Mediated Synthesis of Carbon Nitride: Band-Gap Engineering and Improved Functions for Photocatalysis. *Energy Environ. Sci.* **2011**, *4* (3), 675–678. DOI: 10.1039/C0EE00418A.

(38) Dong, G.; Zhang, Y.; Pan, Q.; Qiu, J. A Fantastic Graphitic Carbon Nitride (g-C3N4) Material: Electronic Structure, Photocatalytic and Photoelectronic Properties. *J. Photochem. Photobiol. C Photochem. Rev.* **2014**, *20*, 33–50. DOI: 10.1016/J.JPHOTOCHEMREV.2014.04.002.

(39) Muñoz-Batista, M. J.; Nasalevich, M. A.; Savenije, T. J.; Kapteijn, F.; Gascon, J.; Kubacka, A.; Fernández-García, M. Enhancing Promoting Effects in G-C3N4-Mn+/CeO2-TiO2 Ternary Composites: Photo-Handling of Charge Carriers. *Appl. Catal. B Environ.* **2015**, *176–177*, 687–698. DOI: 10.1016/j.apcatb.2015.04.051.

(40) Moulder, J. F.; Sticlke, W. F.; Sobol, P. E.; Bomben, K. D. *Handbook of X-Ray Photoelectron Spectroscopy*; PerkinElmer Corporation: Eden Prairie: MN, 1992.

(41) Kibsgaard, J.; Tsai, C.; Chan, K.; Benck, J. D.; Nørskov, J. K.; Abild-Pedersen, F.; Jaramillo, T. F. Designing an Improved Transition Metal Phosphide Catalyst for Hydrogen Evolution Using Experimental and Theoretical Trends. *Energy Environ. Sci.* **2015**, *8* (10), 3022–3029. DOI: 10.1039/C5EE02179K.

(42) Ji, X.; Liu, B.; Ren, X.; Shi, X.; Asiri, A. M.; Sun, X. P-Doped Ag Nanoparticles Embedded in N-Doped Carbon Nanoflake: An Efficient Electrocatalyst for the Hydrogen Evolution Reaction. *ACS Sustain. Chem. Eng.* **2018**, *6* (4), 4499–4503. DOI: 10.1021/acssuschemeng.7b04732.

(43) Zhao, Y.; Zhao, F.; Wang, X.; Xu, C.; Zhang, Z.; Shi, G.; Qu, L. Graphitic Carbon Nitride Nanoribbons: Graphene-Assisted Formation and Synergic Function for Highly Efficient

Hydrogen Evolution. *Angew. Chemie Int. Ed.* **2014**, *53* (50), 13934–13939. DOI: 10.1002/anie.201409080.

(44) Peng, Y.; Pan, W.; Wang, N.; Lu, J.-E.; Chen, S. Ruthenium Ion-Complexed Graphitic Carbon Nitride Nanosheets Supported on Reduced Graphene Oxide as High-Performance Catalysts for Electrochemical Hydrogen Evolution. *ChemSusChem* **2018**, *11* (1), 130–136. DOI: 10.1002/cssc.201701880.

(45) Liu, Y.; Xu, X.; Zhang, J.; Zhang, H.; Tian, W.; Li, X.; Tade, M. O.; Sun, H.; Wang, S.; Wang, S. Flower-like MoS2 on Graphitic Carbon Nitride for Enhanced Photocatalytic and Electrochemical Hydrogen Evolutions. *Appl. Catal. B Environ.* **2018**, *239*, 334–344. DOI: 10.1016/j.apcatb.2018.08.028.

(46) Qu, K.; Zheng, Y.; Zhang, X.; Davey, K.; Dai, S.; Qiao, S. Z. Promotion of Electrocatalytic Hydrogen Evolution Reaction on Nitrogen-Doped Carbon Nanosheets with Secondary Heteroatoms. *ACS Nano* **2017**, *11* (7), 7293–7300. DOI: 10.1021/acsnano.7b03290.

(47) Bhowmik, T.; Kundu, M. K.; Barman, S. CoFe Layered Double Hydroxide Supported on Graphitic Carbon Nitrides: An Efficient and Durable Bifunctional Electrocatalyst for Oxygen Evolution and Hydrogen Evolution Reactions. *ACS Appl. Energy Mater.* **2018**, *1* (3), 1200–1209. DOI: 10.1021/acsaem.7b00305.

(48) Arif, M.; Yasin, G.; Shakeel, M.; Mushtaq, M. A.; Ye, W.; Fang, X.; Ji, S.; Yan, D. Hierarchical CoFe-Layered Double Hydroxide and g-C_3N_4 Heterostructures with Enhanced Bifunctional Photo/Electrocatalytic Activity towards Overall Water Splitting. *Mater. Chem. Front.* **2019**, *3* (3), 520–531. DOI: 10.1039/C8QM00677F.

(49) Liu, Y.; Zhang, H.; Ke, J.; Zhang, J.; Tian, W.; Xu, X.; Duan, X.; Sun, H.; O Tade, M.;

Wang, S. 0D (MoS_2)/2D (g-C_3N_4) Heterojunctions in Z-Scheme for Enhanced Photocatalytic and Electrochemical Hydrogen Evolution. *Appl. Catal. B Environ.* **2018**, *228*, 64–74. DOI: 10.1016/J.APCATB.2018.01.067.

(50) Alba-Molina, D.; Puente Santiago, A. R. R.; Giner-Casares, J. J.; Rodriguez-Castellon, E.; Martin-Romero, M. T.; Camacho, L.; Luque, R.; Cano, M. Tailoring ORR and HER Electrocatalytic Performances of Gold Nanoparticles through Metal-Ligand Interfaces. J. Mater. Chem. A 2019. DOI: 10.1039/C9TA05492H.

(51) Tran, T. D.; Nguyen, M. T. T.; Le, H. V.; Nguyen, D. N.; Truong, Q. D.; Tran, P. D. Gold Nanoparticles as an Outstanding Catalyst for the Hydrogen Evolution Reaction. Chem. Commun. 2018, 54 (27), 3363–3366. DOI: 10.1039/C8CC00038G.

(52) Beyene, B. B., Mane, S. B., Hung, C. H. Highly efficient electrocatalytic hydrogen evolution from neutral aqueous solution by a water-soluble anionic cobalt (II) porphyrin. Chem. Commun. 2015, 51(81), 15067-15070. DOI: 10.1039/C5CC05582B.

(52) Muñoz-Batista, M. J.; Kubacka, A.; Fernández-García, M. Effective Enhancement of TiO_2 Photocatalysis by Synergistic Interaction of Surface Species: From Promoters to Co-Catalysts. *ACS Catal.* **2014**, *4* (12), 4277–4288. DOI: 10.1021/cs501408u.

Table of Contents (TOC GRAPHIC)

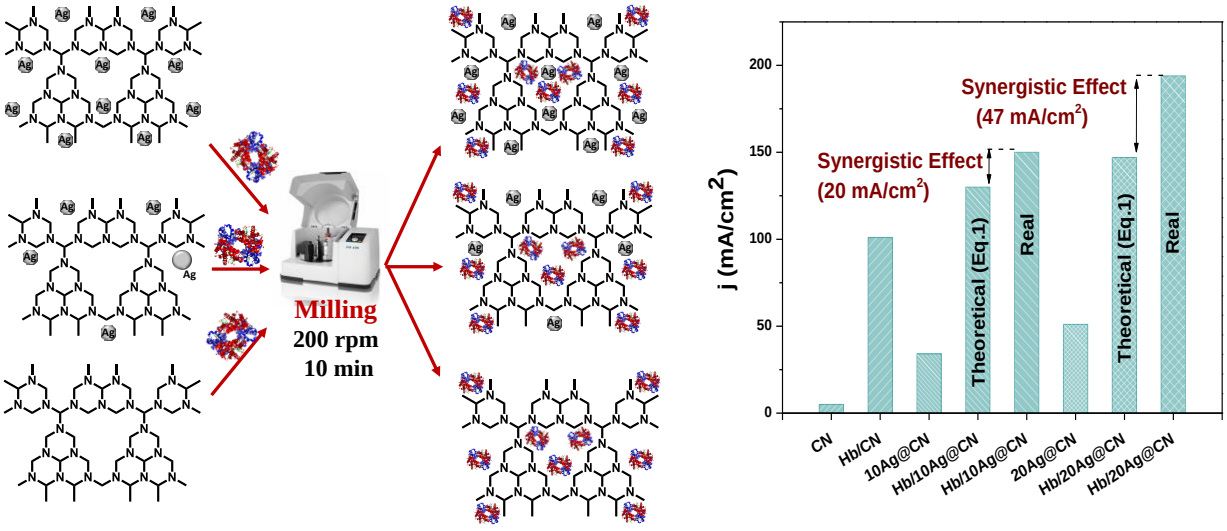

Supporting Information

Improving electrochemical hydrogen evolution of Ag@CN nanocomposites by synergistic effects with α-rich proteins

Daily Rodríguez-Padrón,[a¥] Alain R. Puente-Santiago, [a,b¥] Manuel Cano,[c] Alvaro Caballero,[d] Mario J. Muñoz-Batista,[a,e*] and Rafael Luque[a,f*]

[a] Departamento de Química Orgánica, Universidad de Córdoba, Campus de Rabanales, Edificio Marie Curie (C-3), Ctra Nnal IV-A, Km 396, E14014, Cordoba, Spain.

[b] Department of Chemistry, University of Texas at El Paso, 500 W. University Avenue, El Paso, Texas 79968, United States.

[c] Departamento de Química Física y Termodinámica Aplicada, Instituto Universitario de Nanoquímica (IUNAN), Facultad de Ciencias, Universidad de Córdoba, Campus de Rabanales, Ed. Marie Curie, E-14071 Córdoba, Spain.

[d] Departamento de Química Inorgánica e Ingeniería Química, Instituto Universitario de Investigación en Química Fina y Nanoquímica IUIQFN, Facultad de Ciencias, Universidad de Córdoba, Campus de Rabanales, Ed. Marie Curie, E-14071 Córdoba, Spain.

[e] Department of Chemical Engineering, Faculty of Sciences, University of Granada. Avda. Fuentenueva, s/n 18071, Granada, Spain.

[f] Peoples Friendship University of Russia (RUDN University), 6 Miklukho-Maklaya Str., 117198, Moscow, Russia.

*M.J.M-B. jmunoz385x@gmail.com, *R.L. rafael.luque@uco.es

¥ These authors contribute equally to this work.

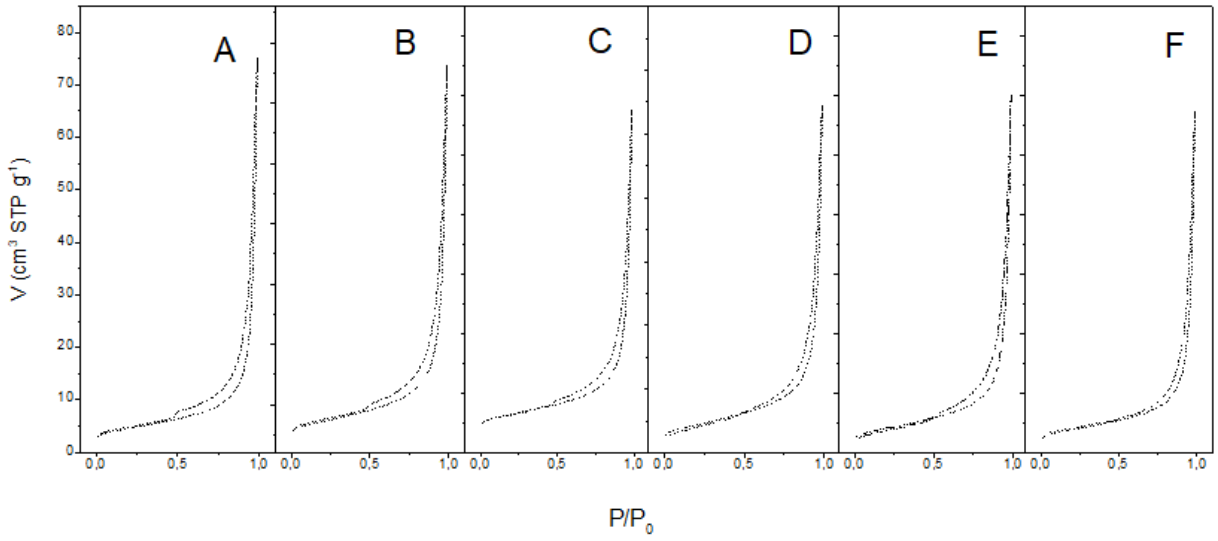

Figure S1. N_2 adsorption-desorption isotherms of A: CN, B: 10%Ag@CN, C: 20%Ag@CN, D: Hb/CN, E: Hb/10%Ag@CN, F: Hb/20%Ag@CN.

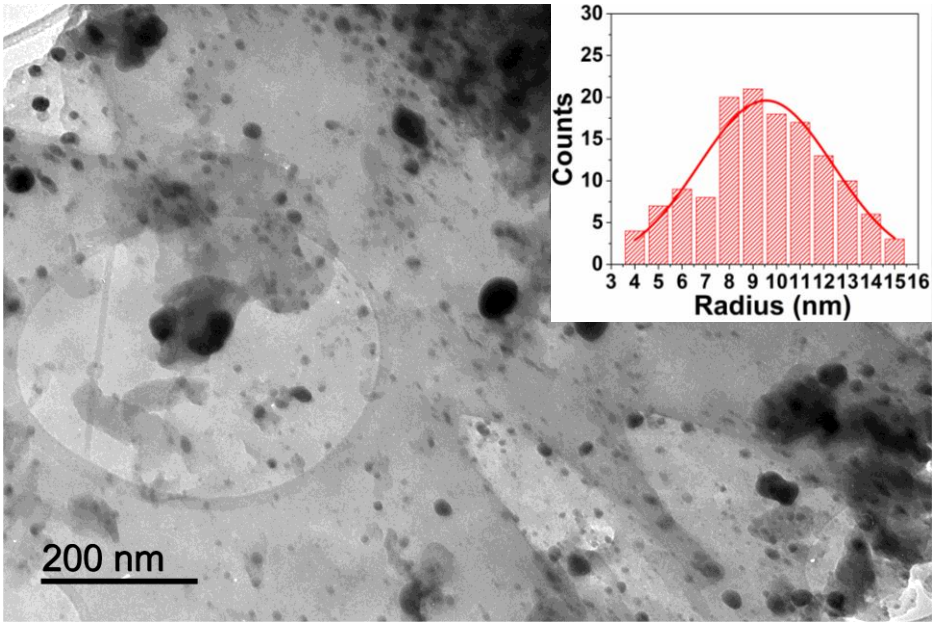

Figure S2. TEM image and particle size distribution of Hb/20Ag@CN material.

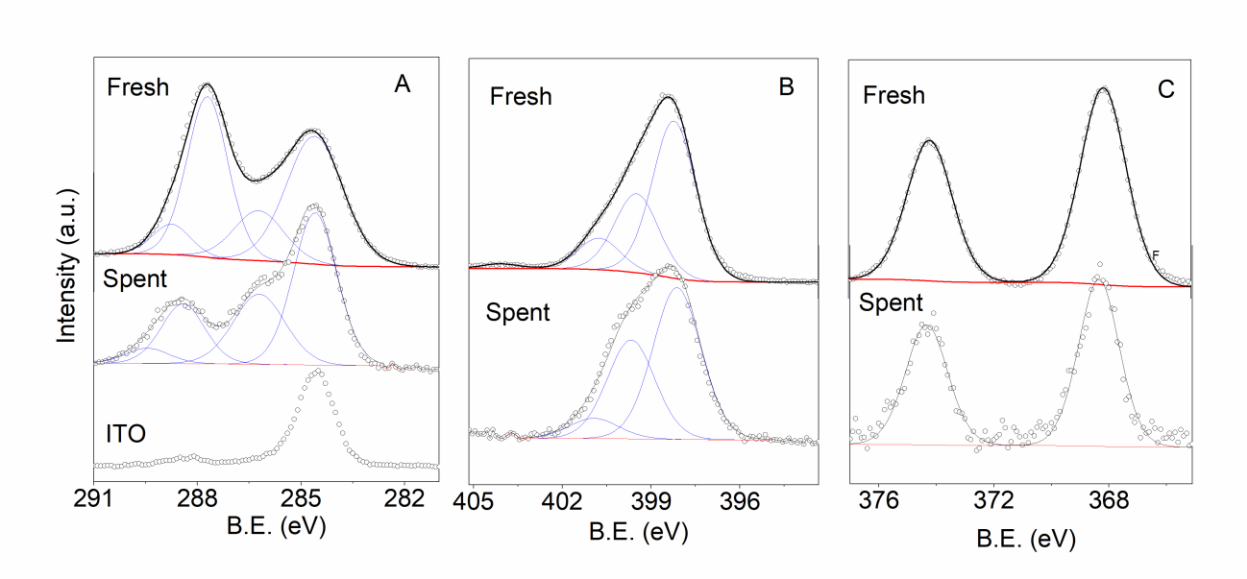

Figure S3. XPS spectra of fresh and spent Hb/20Ag@C_3N_4 in the (A) C1s, (B) N1s and (C) Ag3d regions.

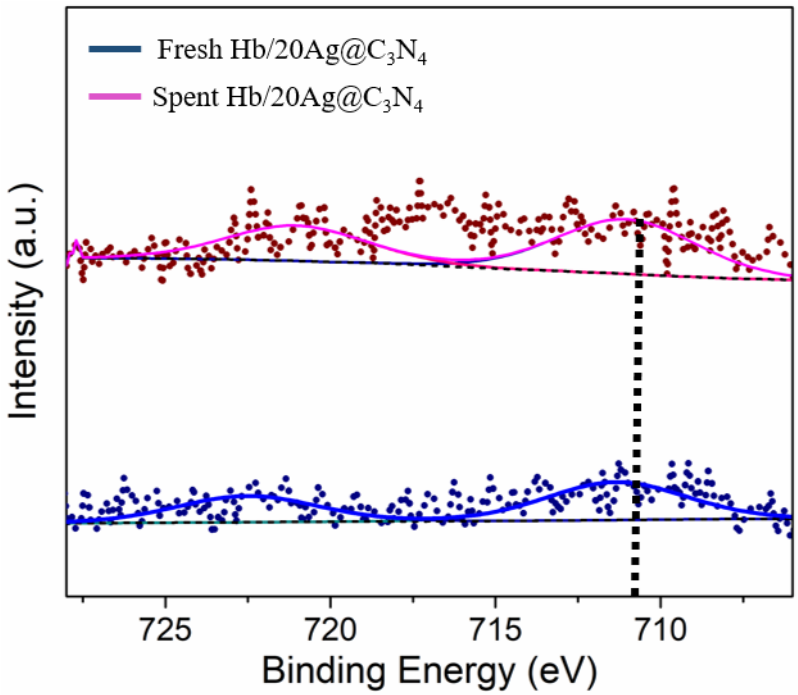

Figure S4. Fe2p XPS spectra of fresh (blue line) and spent catalyst.

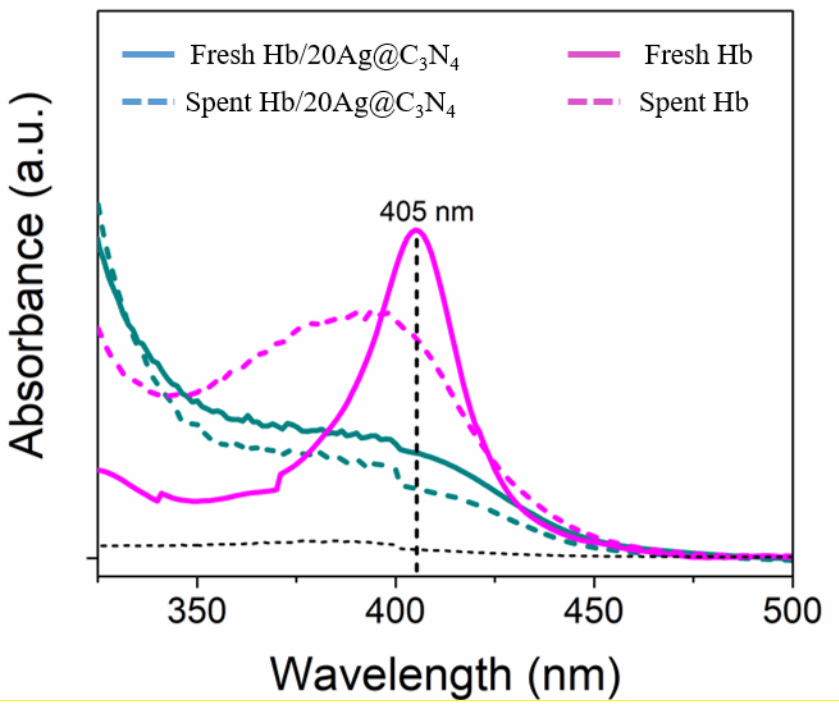

Figure S5. UV spectra of Hb/20Ag@C_3N_4 before and after the electrochemical reaction, and free Hb before and after the electrochemical reaction.